

High-order splitting of non-unitary operators on quantum computers

Peter Brearley^{1,2} and Philipp Pfeffer³

¹*Centre for Quantum Science and Engineering, University of Manchester, UK*

²*Department of Mechanical and Aerospace Engineering, University of Manchester, UK*

³*Institute of Thermodynamics and Fluid Mechanics, Technische Universität Ilmenau, Germany*

Dissipation and irreversibility are central to most physical processes, yet they lead to non-unitary dynamics that are challenging to realise on quantum processors. High-order operator splitting is an attractive approach for simulating unitary dynamics, yet conventional product formulas introduce negative time steps at high orders that are numerically unstable for dissipative dynamics. We show how complex-coefficient product formulas can decompose dissipative dynamics into a sequence of simple Hamiltonian evolutions in real and imaginary time with high-order accuracy. The unitary substages use positive real coefficients, while the dissipative substages use complex coefficients with positive real parts, where the real parts preserve the contractive evolution and the imaginary parts are additional unitary evolutions. We demonstrate the approach by simulating the classical problem of lossy mechanical wave propagation on a trapped-ion quantum processor. A step of order 4 achieves greater accuracy than the steps with low orders 1 and 2, despite the increased circuit depth on noisy hardware. The results suggest that high-order operator splitting is an accurate and practical approach for simulating dissipative dynamics on near-term quantum processors.

I. INTRODUCTION

Quantum computers are naturally suited to simulating unitary dynamics because their native gate model implements the reversible time evolution of local Hamiltonians [1]. In contrast, most problems of practical interest in computational science are dissipative, arising from mechanisms such as friction, viscosity, diffusion, or boundary flux. Even in descriptions of quantum systems, dynamics are invariably coupled to uncontrolled environmental interactions [2], motivating descriptions of dissipative open-system dynamics [3, 4]. Developing accurate and efficient methods for simulating non-unitary, dissipative dynamics on quantum computers is therefore an important step towards supporting the adoption of quantum computing more broadly across computational science.

Operator splitting is a versatile framework for simulating Hamiltonian dynamics on quantum computers [1], and high-order extensions ensure that this versatility does not come at the cost of accuracy [5, 6]. High-order product formulas (beyond order 2) necessarily contain negative coefficients [7, 8], which require simulating the reverse dynamics. This is straightforward for Hamiltonian dynamics, since the reverse evolution is also unitary. For dissipative dynamics, however, the reverse evolution is numerically unstable and cannot be block-encoded into unitary operators without rescaling [9]. High-order operator splitting for the quantum simulation of dissipative dynamics is therefore yet to be demonstrated [10, 11], with existing applications being limited to order 2 [12].

Operator splitting is typically applied to time-evolution problems that can be written as a first-order system of ordinary differential equations (ODEs). In the linear case, this is

$$\frac{d\vec{\psi}}{dt} = M\vec{\psi} \quad (1)$$

for generator M . This system arises from discretising lin-

ear partial differential equations (PDEs) with constant transport coefficients by, for example, the finite difference or Fourier spectral methods. When discretised by N grid points, a temporally m -order PDE becomes an mN -dimensional system of ODEs. Efficient algorithms for integrating Eq. (1) without operator splitting have been proposed [13, 14], but they typically require deep circuits even for simple problems [15], so are not viable strategies for near-term quantum computing.

To simulate Eq. (1) by operator splitting, we consider the decomposition of M into its Hermitian and anti-Hermitian components by $M = H_1 + iH_2$, where $H_1 = H_1^\dagger$ and $H_2 = H_2^\dagger$. For purely dissipative dynamics, such as diffusion or damping, then $M = M^\dagger$ is naturally Hermitian and has real, non-positive eigenvalues. For unitary dynamics, such as advection or wave propagation, then $M = -M^\dagger$ is naturally anti-Hermitian and has imaginary eigenvalues. Therefore, in many systems, the physics described by the individual terms of the PDE naturally separates M into Hermitian H_1 and anti-Hermitian iH_2 components. For systems where the dynamics do not naturally separate, they can be manually separated [13, 14] by defining

$$H_1 = \frac{M + M^\dagger}{2}, \quad iH_2 = \frac{M - M^\dagger}{2}. \quad (2)$$

This extends to systems of inhomogeneous ODEs of the form $d_t \vec{\psi} = M\vec{\psi} + \vec{b}$, which can be homogenised by a simple block-matrix construction [14].

Equation (1) has the solution $\vec{\psi}(t) = e^{Mt}\vec{\psi}(0)$, which can equivalently be written as $\vec{\psi}(t) = e^{H_1 t + iH_2 t}\vec{\psi}(0)$ by Eq. (2). The split evolution $e^{iH_2 t}e^{H_1 t}$ is only equal to $e^{H_1 t + iH_2 t}$ if H_1 and H_2 commute, i.e. $[H_1, H_2] = 0$. This occurs for dynamics that simultaneously diagonalise in the same basis, which often also admit analytical solutions [12]. Therefore, operator splitting is generally required for non-trivial problems.

The order-1 Lie-Trotter splitting is defined as

$$e^{H_1 t + i H_2 t} = (e^{i H_2 \Delta t} e^{H_1 \Delta t})^{t/\Delta t} + O(\Delta t), \quad (3)$$

and the order-2 Strang splitting is defined as

$$e^{H_1 t + i H_2 t} = \left(e^{i H_2 \frac{\Delta t}{2}} e^{H_1 \Delta t} e^{i H_2 \frac{\Delta t}{2}} \right)^{t/\Delta t} + O(\Delta t^2), \quad (4)$$

where the overall evolution by time t is discretized into $t/\Delta t \in \mathbb{N}$ steps of size Δt . Improving on the order-1 splitting in Eq. (3) to the order-2 splitting in Eq. (4) is straightforward, as it requires simulating one evolution between two half-steps of the other, and yields a substantial improvement in accuracy.

The evolutions by $e^{H_1 t}$ and $e^{i H_2 t}$ are usually much simpler to implement on quantum computers than $e^{H_1 t + i H_2 t}$, as they represent reduced mechanisms of the dynamics. Furthermore, problems of this type have been extensively studied in the context of Hamiltonian simulation [16] and imaginary time evolution [17, 18] algorithms. If they cannot be implemented directly, then H_1 and H_2 can be further decomposed into sums of simpler Hamiltonians that can be efficiently simulated, and incorporated into Eq. (3) or (4) by recursively applying the respective product formula. Therefore, operator splitting is a practical means of simulating general non-unitary dynamics on quantum computers [12], but its usefulness is severely limited by the accuracy of Eqs. (3) and (4), which require deep circuits to converge to within a reasonable tolerance for most practical systems.

In this work, we demonstrate a stable quantum algorithm for integrating non-unitary dynamics on quantum computers by high-order operator splitting. We do this by considering product formulas with complex coefficients a_j satisfying $\Re(a_j) > 0$ for the dissipative evolution and real coefficients $b_j > 0$ for the unitary evolution. The coefficients ensure that the unitary and dissipative dynamics are both retained in the real-time evolution, while the dissipative dynamics evolving in imaginary time become unitary. Therefore, the dynamics of the overall system can be decomposed into a sequence of simple Hamiltonians evolving in real and imaginary time. The approach produces a direct, unscaled block encoding of the dissipative evolution operator to a chosen high order of accuracy. The method presently allows orders up to 6 to be obtained, using the highest-order qualifying product formulas that have been reported in the literature [19].

In the next section, *High-Order Operator Splitting*, the qualifying high-order product formulas of orders 4 and 6 are presented. We then give a practical demonstration in *Application to Damped Waves*, where quantum circuits for simulating the classical damped wave equation using the proposed approach are derived, validated in statevector simulations, and executed on the IonQ Forte 1 trapped-ion quantum processor [20]. In *Resource Requirements*, the gate complexity in the general case and the exact CNOT gate count in the applied case are de-

rived. The conclusions and opportunities for future work are discussed in the final section, *Conclusions*.

II. HIGH-ORDER OPERATOR SPLITTING

A p -order product formula $\Phi_p(t, \Delta t)$ for simulating the linear dynamics in Eq. (1) satisfies

$$e^{Mt} = \Phi_p(t, \Delta t) + O(\Delta t^p), \quad (5)$$

comprising q stages and $t/\Delta t \in \mathbb{N}$ steps such that

$$\Phi_p(t, \Delta t) = (S_{q-1} \cdots S_1 S_0)^{t/\Delta t}, \quad (6)$$

where S_j is a stage in the splitting step. We utilise complex-coefficient product formulas to evolve Eq. (1) for $M = H_1 + i H_2$ given by Eq. (2). The dissipative substages $e^{H_1 a_j \Delta t}$ are evolved by complex coefficients a_j satisfying $\Re(a_j) > 0$, and the unitary substages $e^{i b_j H_2 \Delta t}$ are evolved by real coefficients $b_j > 0$. The complex coefficients a_j are scalars, so the real and imaginary components commute and can therefore be implemented sequentially with no additional error. An individual stage S_j can therefore be defined as

$$S_j(\Delta t) = e^{i H_2 b_j \Delta t} e^{i H_1 \Im(a_j) \Delta t} e^{H_1 \Re(a_j) \Delta t}. \quad (7)$$

Each of the substages in Eq. (7) are typically much simpler to realise on a quantum computer than the exact evolution $e^{H_1 t + i H_2 t}$. If the implementation remains challenging, the evolution can be further split by decomposing the Hamiltonians $H_1 = \sum_k A_k$ and $H_2 = \sum_k B_k$ into sums of simpler Hamiltonians A_k and B_k that can be efficiently simulated. This requires the recursive use of product formulas that match the overall order being targeted. The two unitary substages in Eq. (7), $e^{i H_2 b_j \Delta t}$ and $e^{i H_1 \Im(a_j) \Delta t}$, can be split with high-order real-coefficient product formulas, which can be constructed systematically to arbitrary accuracy [23]. The dissipative substage in Eq. (7), $e^{H_1 \Re(a_j) \Delta t}$, requires each A_k to be negative semi-definite and split using complex-coefficient product formulas with positive real parts. For this purpose, we can use two complex coefficients where both real parts are positive, which can also be constructed systematically to arbitrary order [24].

A product formula that satisfies the imposed constraints of $\Re(a_j) > 0$ and $b_j > 0$ was shown by Castella *et al.* [22] and approximates the evolution $e^{H_1 t + i H_2 t}$ to order 4 with 5 stages. It uses the positive real coefficient $b_j = 1/4$ across four of the stages $j = 0, 1, 2, 3$. The dissipative dynamics evolve under complex coefficients with positive real parts $a_0 = 1/10 - i/30$, $a_1 = 4/15 + 2i/15$, $a_2 = 4/15 - i/5$, $a_3 = a_1$ and $a_4 = a_0$. The dynamics can then be simulated by Eqs. (5–7).

Two order-6 product formulas under the same constraints of $\Re(a_j) > 0$ and $b_j > 0$ were presented by Bernier *et al.* [19], consisting of 12 or 16 stages. In this work, we proceed with the 16-stage scheme due to its

TABLE I. Product formulas with coefficients $a_j \in \mathbb{C}$ and $b_j \in \mathbb{R}$, where $\Re(a_j) > 0$ and $b_j > 0$. A superscript star denotes the complex conjugate.

Product formula	Complex coefficient a_j	Real coefficient b_j
Lie-Trotter (order 1)	$a_0 = 1$	$b_0 = 1$
Strang [21] (order 2)	$a_0 = a_1 = 1/2$ (or $a_0 = 1$)	$b_0 = 1$ (or $b_0 = b_1 = 1/2$)
Castella <i>et al.</i> [22] (order 4)	$a_0 = a_4 = 1/10 - i/30$ $a_1 = a_3 = 4/15 + 2i/15$ $a_2 = 4/15 - i/5$	$b_0 = b_1 = b_2 = b_3 = 1/4$
Bernier <i>et al.</i> [19] (order 6)	$a_0 = a_{15}^* = 0.03 - 0.0028985018717006387i$ $a_1 = a_{14}^* = 0.08826477458499815 + 0.019065371639195743i$ $a_2 = a_{13}^* = 0.07026507350715319 - 0.05226928459003309i$ $a_3 = a_{12}^* = 0.051044248093469226 + 0.075802626396177709i$ $a_4 = a_{11}^* = 0.040506044227148555 - 0.07981221177569087i$ $a_5 = a_{10}^* = 0.03061653536468681 + 0.07254698089135206i$ $a_6 = a_9^* = 0.10349890449629792 - 0.03539199012223482i$ $a_7 = a_8^* = 0.08580441972624608 + 0.011182129837497105i$	$b_0 = b_{14} = 0.08092666015955027$ $b_1 = b_{13} = 0.06736427978832901$ $b_2 = b_{12} = 0.057276240999706116$ $b_3 = b_{11} = 0.06428730473896961$ $b_4 = b_{10} = 0.05528732144478408$ $b_5 = b_9 = 0.02566179136566552$ $b_6 = b_8 = 0.10559039215618958$ $b_7 = 0.08721201869361150$

more balanced coefficients, which lead to a more reliable order-6 convergence across larger steps in practice. The coefficients of all product formulas used in this study are shown in Table I.

Both high-order product formulas satisfy our constraints of $\Re(a_j) > 0$ and $b_j > 0$, yet they belong to different symmetry classes. The order-4 method of Castella *et al.* [22] is palindromic, whereas the order-6 method of Bernier *et al.* [19] is symmetric-conjugate. Symmetric-conjugate product formulas were originally devised for the classical simulation of unitary dynamics, as they preserve reversibility under complex conjugation [19]. For our application, we found no reason to prefer one class over the other.

To the best of our knowledge, the order-6 product formulas presented by Bernier *et al.* [19] are the highest-order qualifying formulas that have been reported in the literature. There is no known deterministic method of producing such coefficients besides numerical searches that solve the polynomial order conditions from many random initialisations [19]. In principle, the presented technique can be applied to any product formula with coefficients satisfying $a_j \in \mathbb{C}$ and $b_j \in \mathbb{R}$ with $\Re(a_j) > 0$. The coefficients in Table I are subject to the additional constraint of $b_j > 0$. This is a desirable property, since more balanced coefficients lead to faster convergence in practice, but it is not strictly necessary for our application. Relaxing this constraint may ease the discovery of coefficients with order 8 and beyond. This is of theoretical interest, although orders 4 and 6 will be preferred in many scenarios since the number of coefficients grows exponentially with the order of the product formula [25].

III. APPLICATION TO DAMPED WAVES

We use the example from classical physics of a linearly damped wave to demonstrate the approach, which is modelled by

$$\frac{\partial^2 \psi}{\partial t^2} + \gamma \frac{\partial \psi}{\partial t} = c^2 \nabla^2 \psi \quad (8)$$

for damping coefficient γ and wave speed c . We have chosen an example with a non-trivial quantum circuit derivation to show how the approach can be applied in practice. We then simulate the derived circuits in statevector simulations to validate the accuracy, and on the IonQ Forte 1 trapped-ion quantum processor [20] to assess the feasibility for near-term applications.

A. Quantum Circuit Derivation

Applying the Fourier transform to Eq. (8) in one dimension, then adopting a pseudo-spectral discretisation by N modes corresponding to N discrete grid points, each mode evolves under

$$\frac{d^2}{dt^2} \hat{\psi}_j + \gamma \frac{d}{dt} \hat{\psi}_j + \omega_j^2 \hat{\psi}_j = 0. \quad (9)$$

This is the damped oscillator ODE, where mode j has wavenumber k_j and oscillates with an angular frequency $\omega_j = c|k_j|$ in the undamped case, or $\sqrt{\omega_j^2 - \gamma^2/4}$ in the damped case. It can be written as the first-order system

$$\frac{d}{dt} \begin{bmatrix} \hat{\psi}_j \\ d_t \hat{\psi}_j / \omega_j \end{bmatrix} = \left(\underbrace{\begin{bmatrix} 0 & \omega_j \\ -\omega_j & 0 \end{bmatrix}}_{i\omega_j Y} + \underbrace{\begin{bmatrix} 0 & 0 \\ 0 & -\gamma \end{bmatrix}}_{-\gamma|1\rangle\langle 1|} \right) \begin{bmatrix} \hat{\psi}_j \\ d_t \hat{\psi}_j / \omega_j \end{bmatrix}, \quad (10)$$

where $Y = -i|0\rangle\langle 1| + i|1\rangle\langle 0|$ is the Pauli-Y gate. The exact evolution is governed by $e^{i\omega_j Y t - \gamma|1\rangle\langle 1|t}$, which has a cumbersome closed-form and a nonlinear dependence on ω_j , with no readily apparent quantum circuit decomposition. If we instead consider the split dynamics, then $e^{i\omega_j Y t} = R_Y^\dagger(2\omega_j t)$ and $e^{-\gamma|1\rangle\langle 1|t} = |0\rangle\langle 0| + e^{-\gamma t}|1\rangle\langle 1|$, where $R_Y(\theta) = e^{-i\frac{\theta}{2}Y}$ is the standard quantum gate that rotates about y axis of the Bloch sphere, and $R_Y^\dagger(\theta) = R_Y(-\theta)$ is its inverse. Hence, operator splitting simplifies the non-trivial dynamics of $e^{i\omega_j Y t - \gamma|1\rangle\langle 1|t}$ in terms of a standard quantum gate and a simple non-unitary operator that can be readily implemented.

Equation (10) describes the evolution of a single mode, while in practice, we need a quantum circuit that evolves a statevector containing all modes simultaneously. For this, the quantum amplitudes are prepared either in Fourier space as

$$|\hat{\Psi}\rangle \propto \sum_{j=0}^{N-1} \left(\hat{\psi}_j |0\rangle_S + \frac{d_t \hat{\psi}_j}{\omega_j} |1\rangle_S \right) \otimes |j\rangle_D, \quad (11)$$

or in physical space as

$$|\Psi\rangle \propto \sum_{j=0}^{N-1} (\psi_j |0\rangle_S + |c\partial_x|^{-1} \partial_t \psi_j |1\rangle_S) \otimes |j\rangle_D, \quad (12)$$

followed by the quantum Fourier transform. Since $\omega_0 = 0$, then $d_t \hat{\psi}_0 / \omega_0$ must be handled separately, and can be set to 0 for waves with a velocity that has a zero spatial mean. The initial condition is encoded into the data register $|\text{dat}\rangle_D$ with the selector qubit $|\text{sel}\rangle_S$ distinguishing between the vertical wave displacement and the velocity.

To derive the circuit, we decompose ω_j using the binary expansion of its index $j = \sum_{r=0}^{n-1} 2^r q_r$, where $q_r \in \{0, 1\}$ is qubit r , q_0 is the least-significant qubit, and $N = 2^n$. Considering the periodic boundary conditions that are enforced by the QFT, the wavenumber defined on a domain of length L is $k_j = 2\pi j/L$ when $0 \leq j < N/2$, and $k_j = (2\pi/L)(j - N)$ when $N/2 \leq j < N$. Therefore, $\omega_j = c|k_j|$ can be expanded to

$$\omega_j = \frac{2\pi c}{L} \begin{cases} \sum_{r=0}^{n-1} 2^r q_r, & 0 \leq j < 2^{n-1} \\ 2^n - \sum_{r=0}^{n-1} 2^r q_r, & 2^{n-1} \leq j < 2^n. \end{cases} \quad (13)$$

Substituting the expression into the mode evolution operator gives

$$R_Y^\dagger(2\omega_j t) = \begin{cases} R_Y^\dagger\left(\zeta t \sum_{r=0}^{n-1} 2^r q_r\right), & 0 \leq j < 2^{n-1} \\ R_Y^\dagger\left(\zeta t \left[2^n - \sum_{r=0}^{n-1} 2^r q_r\right]\right), & 2^{n-1} \leq j < 2^n, \end{cases} \quad (14)$$

where $\zeta = 4\pi c/L$ is defined for convenience. Using additivity of rotation angles, this becomes

$$R_Y^\dagger(2\omega_j t) = \begin{cases} \prod_{r=0}^{n-1} R_Y^\dagger(2^r \zeta t q_r), & 0 \leq j < 2^{n-1} \\ R_Y^\dagger(2^n \zeta t) \prod_{r=0}^{n-1} R_Y^\dagger(-2^r \zeta t q_r), & 2^{n-1} \leq j < 2^n, \end{cases} \quad (15)$$

which is in terms of R_Y^\dagger gates acting on the $|\text{sel}\rangle_S$ register, controlled by qubits in the $|\text{dat}\rangle_D$ register specified by q_r .

The piecewise dependence can be implemented by conditioning each argument by the most-significant qubit q_{n-1} , which is $|0\rangle$ for $0 \leq j < 2^{n-1}$ and $|1\rangle$ for $2^{n-1} \leq j < 2^n$. Since both expressions in Eq. (15) contain the common product term, $R_Y(\pm 2^r \zeta t q_r)$ up to the sign of the angle, they can be implemented with a positive sign across all j indices, then surrounded by CNOT gates to reverse the sign for the $q_{n-1} = |1\rangle$ component. This avoids the need for additional zero- and one-controlling operations, so all gates are controlled by at most one qubit. Finally, the remaining gate of $R_Y^\dagger(2^n \zeta t)$ can be applied to $2^{n-1} \leq j < 2^n$ by controlling on $q_{n-1} = |1\rangle$. The quantum circuit that implements the evolution is shown in Fig. 1a.

The damping evolution $|0\rangle\langle 0| + e^{-\gamma t}|1\rangle\langle 1|$ applies an exponential decay to the velocity component of the state uniformly across all wavenumbers. It can be implemented by applying

$$\begin{aligned} R(\gamma t) &= R_Y(2 \arccos[e^{-\gamma t}]) \\ &= \begin{bmatrix} e^{-\gamma t} & -\sqrt{1 - e^{-2\gamma t}} \\ \sqrt{1 - e^{-2\gamma t}} & e^{-\gamma t} \end{bmatrix} \end{aligned} \quad (16)$$

to an ancilla qubit in a computational basis state, either $|0\rangle$ or $|1\rangle$, and controlled by $|\text{sel}\rangle_S$. Measuring the ancilla qubit in the same basis state performs the desired evolution.

The quantum circuit that simulates the order 1 splitting step in Eq. (3) is shown in Fig. 1b, which implements the circuits for wave propagation and damping sequentially for a time step Δt . The damping operator is realised by postselection, as here we focus on minimising the circuit depth of a single shot. Alternatively, amplitude amplification [26] may be applied to boost the success probability, but at the cost of an increased circuit depth per shot. The quantum circuit for the order-2 Strang product formula is shown in Fig. 1c, where the damping is evolved for time Δt between wave evolutions for time $\Delta t/2$. We chose this configuration as it only requires a single measurement of the ancilla qubit. The quantum circuit for order 4 [22] using the product formula in Table I is shown in Fig. 1d. The ancilla qubits in the presented circuit may be a single qubit subject to mid-circuit measurements, or different qubits that are all measured at the end of the computation. The same circuit structure in Fig. 1d can be applied to the order 6 splitting, which we have not shown explicitly.

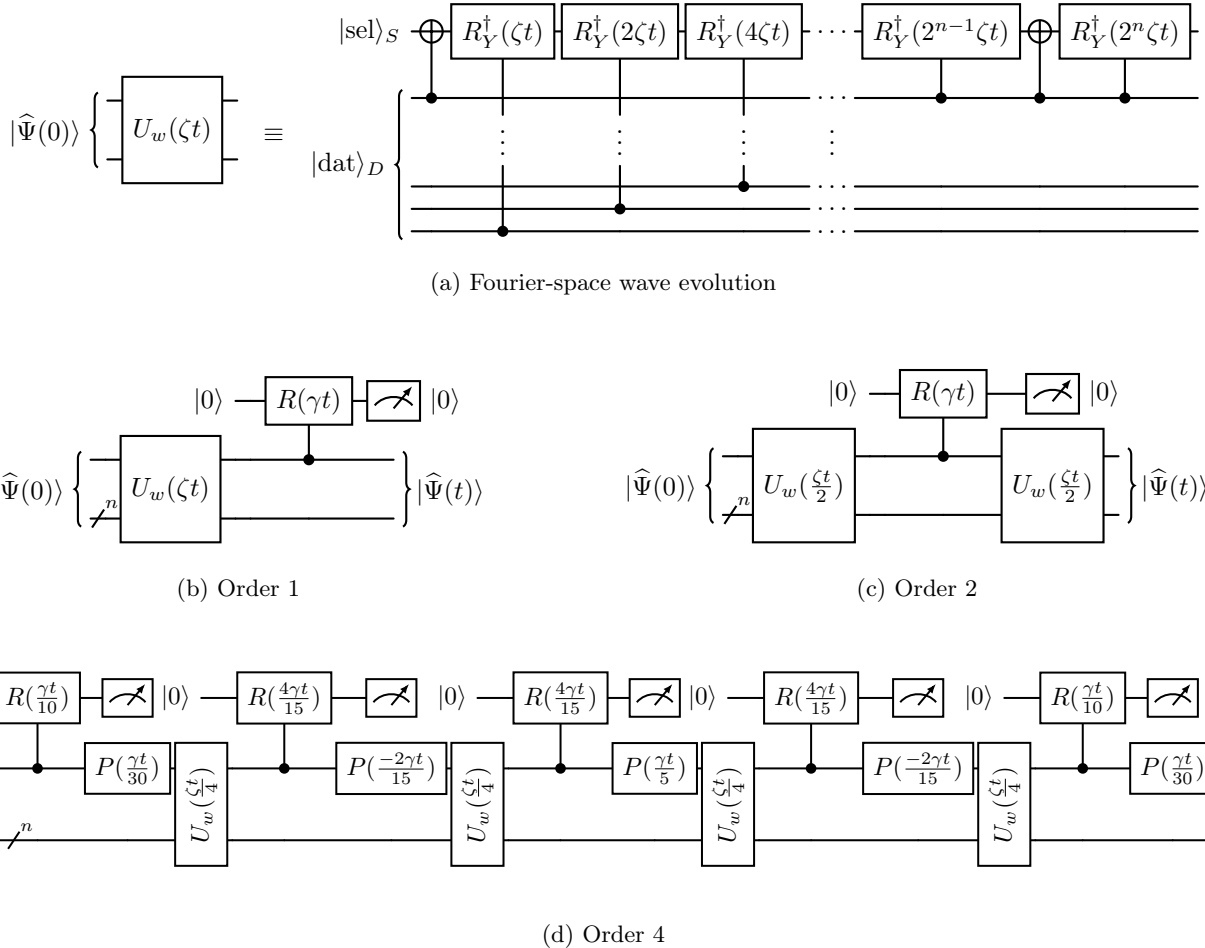


FIG. 1. (a) Quantum circuit for solving the wave equation in Fourier space using the initial state in Eq. (11), where $\zeta = 4\pi c/L$. (b-d) Quantum circuits for simulating one splitting step of size t for the damped wave equation in Fourier space with orders 1, 2 and 4. $P(\theta) = |0\rangle\langle 0| + e^{i\theta}|1\rangle\langle 1|$ is the phase gate, and $R(\theta)$ is an $Ry(\theta)$ gate with a modified argument defined in Eq. (16). The circuits use big-endian ordering.

The circuits for implementing high-order operator splitting use the same constructions of the wave propagation and the real-time damping. The imaginary-time damping $e^{iH_1\Im(a_j)\Delta t} = |0\rangle\langle 0| + e^{-i\gamma\Im(a_j)\Delta t}|1\rangle\langle 1|$ is unitary, corresponding to the phase gate $P(\theta) = |0\rangle\langle 0| + e^{i\theta}|1\rangle\langle 1|$ with $\theta = -\gamma\Im(a_j)\Delta t$ applied to the selector qubit.

In d dimensions, the wave equation evolves under the square root of the sum of the squared wavenumber components as $c\|\vec{k}\|$, so the derived operators for evolving in each dimension do not commute. This is a natural extension of the presented approach, and can be simulated by decomposing $H_2 = \sum_{k=1}^d B_k$ into a Hamiltonian for each spatial dimension. The evolution $e^{iH_2 b_j \Delta t}$ can then be approximated by a high-order real-coefficient product formula [23] to match the target order.

The circuits can be extended to homogeneous Dirichlet or Neumann boundary conditions by using the sine or cosine Fourier bases [27], respectively, which also have efficient quantum circuit implementations [28]. The

wavenumber is then simply $k_j = \pi j/L$ for Neumann conditions or $k_j = \pi(j+1)/L$ for Dirichlet conditions. This was shown by Pfeffer *et al.* [12] in the context of the advection-diffusion equation in a laminar shear flow, by implementing Neumann boundary conditions with the quantum cosine transform corresponding to a thermally insulated wall. This is a further industrial application of the present approach.

B. Statevector Simulations

Figure 2 presents quantum statevector simulations of the algorithm applied to the damped wave equation on a periodic domain of length L . We consider a Gaussian initial condition of $\psi(x, 0) = \exp(-100[x/L - 0.5]^2)$ with a zero initial time derivative so $|\partial_x|^{-1}\partial_t\psi(x, 0) = 0$. The domain is discretised with 128 grid points, and we assume access to a quantum state encoding this function by Eq. (12). This requires $n = 7$ qubits in the data regis-

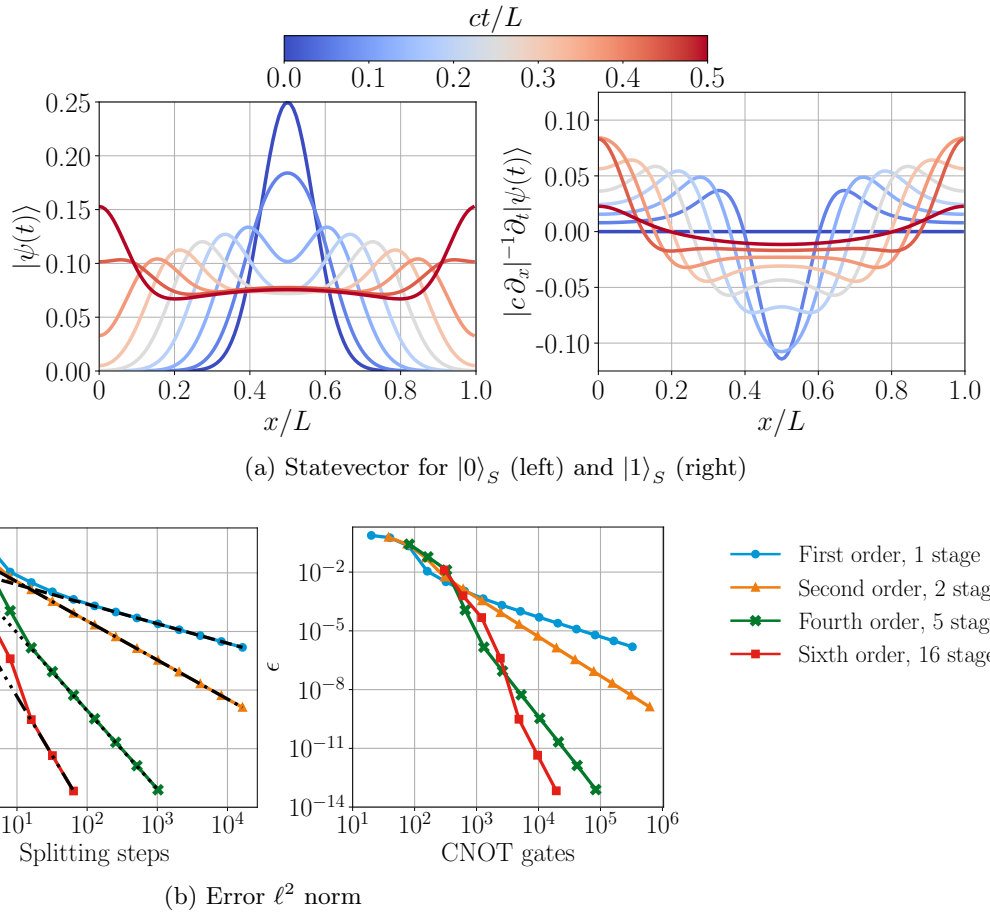


FIG. 2. (a) Statevector simulations of the damped wave equation evolution using nine qubits and eight order-4 splitting steps, with plots showing the physical-space quantities corresponding to the QFT^\dagger applied to the $|dat\rangle_D$ register. (b) The error norm $\epsilon = \|\psi(t)\rangle - \tilde{\psi}(t)\|$ in terms of the number of splitting steps and the number of CNOT gates, where the analytical time-evolution vector $\tilde{\psi}(t)$ was evaluated by $e^{i\omega_j Yt - \gamma|1\rangle\langle 1|t}$ on the same grid, then rescaled to have a unit norm.

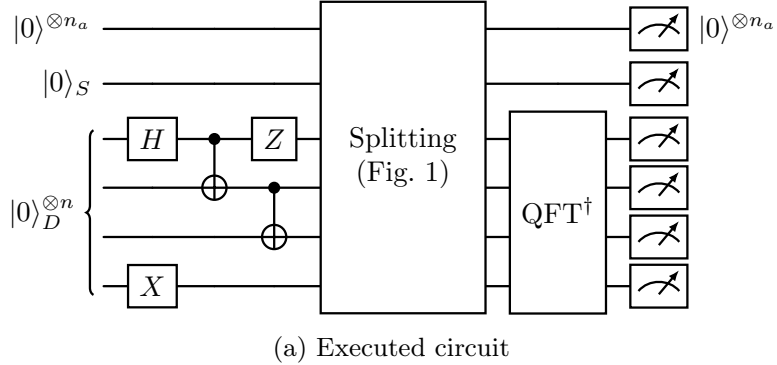
ter, one selector qubit and one ancilla qubit, for a total of nine qubits. The ratio of the wave propagation to damping time scales is $\gamma L/c = 0.5$. Eight order-4 steps are implemented in Fig. 2a, each requiring 82 CNOT gates for a total of 656 CNOT gates to simulate the entire evolution in Fourier space. This calculation and its scaling will be expanded upon in the following *Resource Requirements* section. The cumulative success probability of measuring $|0\rangle$ after each damping stage is approximately 27.6%, corresponding to the squared ratio of the ℓ^2 norm of the unnormalised solution at the final and initial states, $\|\psi(t)\|^2/\|\psi(0)\|^2$.

The exact propagator for the Fourier modes can be obtained by evaluating $e^{i\omega_j Yt - \gamma|1\rangle\langle 1|t}$ classically, which we use to validate the theoretical orders of accuracy with the error ℓ^2 norm. The statevector simulations in Fig. 2a, which use eight order-4 splitting steps, have an error norm of $\epsilon = 1.16 \times 10^{-4}$, evaluated by $\epsilon = \|\psi(t)\rangle - \tilde{\psi}(t)\|$ where the analytical time-evolution vector $\tilde{\psi}(t)$ is scaled to have a unit norm. This error is plotted in Fig. 2b for all product formulas in Table I, against the number

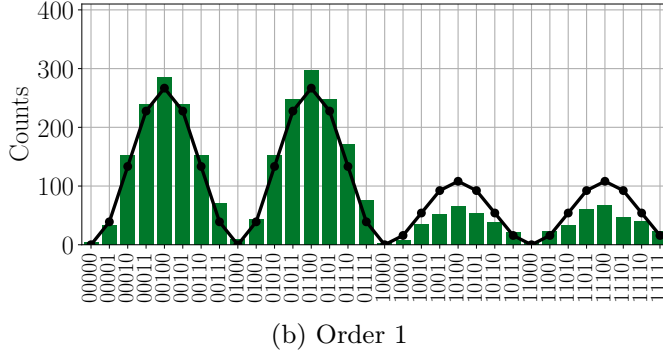
of splitting steps and the number of CNOT gates. The results show that all product formulas achieve the theoretical error scaling after the initial coarse-grid transients have passed. The number of CNOT gates is comparable at large error tolerances, but the higher-order product formulas rapidly become more efficient for small error tolerances. This suggests that there is little disadvantage in using higher-order product formulas up to order 6, even when low-accuracy solutions are permissible. The order-6 splitting achieves the classical machine precision of the emulator with approximately 10^4 CNOT gates.

C. End-to-End Hardware Execution

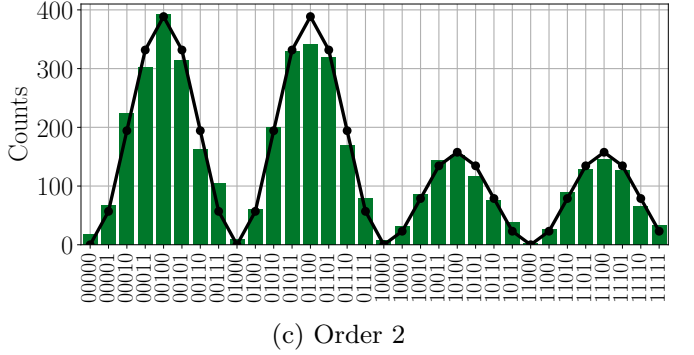
We evaluate the developed high-order product formulas on the IonQ Forte 1 [20], which has 36 all-to-all connected trapped-ion qubits, using the damped wave equation as the example. The full end-to-end execution must be considered, including state preparation. To minimise the number of gates required for state preparation, we



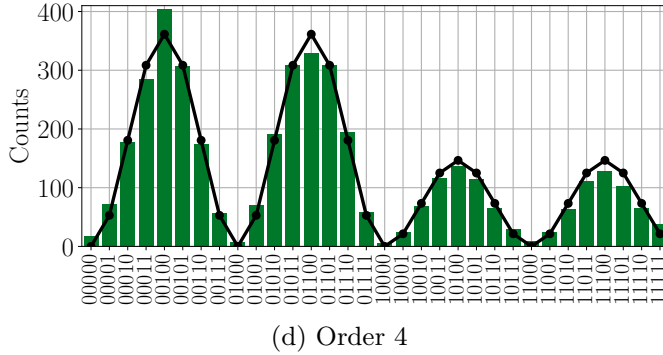
(a) Executed circuit



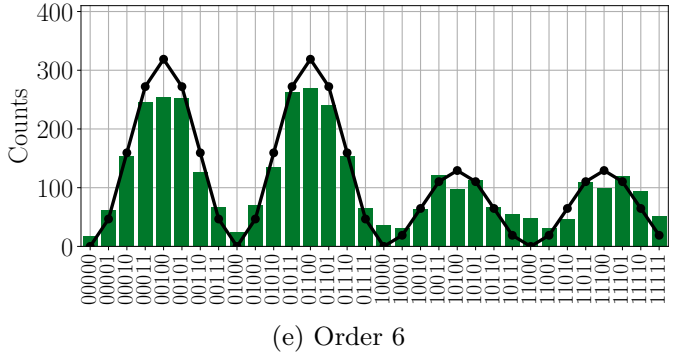
(b) Order 1



(c) Order 2



(d) Order 4



(e) Order 6

FIG. 3. (a) End-to-end quantum circuit for performing a single splitting step with the initial condition in Eq. (17), using the splitting circuits in Fig. 1. (b–e) Measurement histograms from the IonQ Forte 1 for orders 1, 2, 4 and 6 with the expected measurements from the exact, unsplit solution shown by the black line.

prepare a sparse state directly in Fourier space as

$$|\widehat{\Psi}\rangle = |0\rangle_S \otimes \frac{1}{\sqrt{2}}(|1\rangle_D - |N-1\rangle_D), \quad (17)$$

which corresponds to the physical-space amplitudes

$$|\Psi\rangle \propto \sum_{j=0}^{N-1} \sin(2\pi j/N) |0\rangle_S \otimes |j\rangle_D. \quad (18)$$

Therefore, the Fourier modes correspond to an initial displacement described by a periodic sine wave, with a zero initial velocity. This is a standing wave initialised at its maximum displacement. By preparing the state directly in Fourier space, we also avoid the need for the initial QFT. After evolving the state in Fourier space, we then

complete one full inverse QFT to demonstrate that QFT implementation is not prohibitive. The end-to-end quantum circuit is shown in Fig. 3a.

The ratio of wave propagation to damping time scales is again taken to be $\gamma L/c = 0.5$. We use $N = 16$ grid points corresponding to $n = 4$ data-register qubits, with one selector qubit required to store both the displacement and velocity data. To avoid mid-circuit measurements, which can be a dominant source of error on noisy hardware [29], we use a new ancilla qubit for each application of damping in Fig. 1b–d and perform all measurements at the end of the computation. Therefore, the end-to-end execution of a splitting step for orders 1, 2, 4 and 6 requires a total of 6, 6, 10 and 21 qubits and 34, 46, 78 and 232 CNOT gates, respectively, including six CNOT gates

to perform SWAP operations after the inverse QFT. We simulate the problem for one splitting step over the non-dimensional time $ct/L = 0.125$, corresponding to $1/8$ of a full cycle. At this point in the cycle, the undamped evolution has a wave displacement and scaled velocity of equal magnitude, so the effects of damping can be easily visualised.

The histogram of measurement outcomes conditioned on $|0\rangle^{\otimes n_a}$ is shown in Fig. 3b–e for orders 1, 2, 4 and 6 respectively, along with the expected measurement outcomes from the exact (unsplit) evolution. For all orders of accuracy, the correct qualitative behaviour of squared sine profiles with a greater magnitude of displacement than velocity is obtained. The results for order 1 are visibly inaccurate, while the effects of noise become visible for order 6 due to the increased circuit depth per step. The histograms for orders 2 and 4 both appear to be highly accurate, having found a good compromise between accuracy and circuit depth for this particular configuration.

Each case was simulated for 5000 shots and had a probability of successful postselection of 59.98%, 87.38%, 81.26% and 71.68%. This compares to the expected probabilities from the corresponding statevector simulations of 60.39%, 88.40%, 83.38%, and 83.36%, respectively. The expected probability of the true solution is 83.36%, showing that both high-order product formulas achieve high accuracy in the noise-free statevector simulations. The measurements for order 4 are within 2.10% of the true probability, compared to 4.02% for order 2, so the order-4 simulations are more accurate by this metric. Evaluating the error ℓ^2 norm of the reconstructed statevector from the measured data confirms this, resulting in error ℓ^2 norms of 0.1634, 0.1166, 0.1138 and 0.2207 for orders 1, 2, 4 and 6, respectively. Therefore, the results for orders 2 and 4 are of comparable accuracy, with order 4 being slightly more accurate despite the greater susceptibility to noise from the increased circuit depth. For order 6, the effects of noise dominate, resulting in a lower accuracy than the order-1 simulations. The order-4 results highlight the potential of the approach to simulate non-unitary dynamics on near-term quantum processors.

IV. RESOURCE REQUIREMENTS

The required resources for simulating the evolution under a general generator $M = H_1 + iH_2$ will now be analysed, where the unitary and dissipative substages require G_U and G_D CNOT gates, respectively. We then give the expressions for two applications: the classical damped waves presented here, and scalar transport in a laminar shear flow in fluid dynamics [12] that was previously limited to order 2.

The required number of splitting steps scales as $t/\Delta t = O(t^{1+1/p}\epsilon^{-1/p})$ for splitting order p , since $\Delta t = O([\epsilon/t]^{1/p})$. Within each splitting step, the required number of stages generally scales exponentially

as $O(2^{p/2})$ for even-order product formulas [25]. When the contributions are combined, the required number of CNOT gates scales as $O(2^{p/2}t^{1+1/p}\epsilon^{-1/p}[G_U + G_D])$ for a single shot.

Without the use of amplitude amplification [26], successful postselection requires $O(Q^2)$ attempts per successful run, where $Q = \|\vec{\psi}(0)\|/\|\vec{\psi}(t)\|$. This can be improved to $O(1)$ using amplitude amplification [26], under the condition that the non-unitary substages in Fig. 1 are applied to unique ancilla qubits without measurement. This is to prepare a single block encoding of the evolution operator, such that the input state remains known, which is a requirement for amplitude amplification [26]. Instead of introducing a new ancilla qubit for each operation as in Fig. 3, which can lead to an unfavourable scaling in the number of qubits, we can instead use a ‘compression gadget’, such as demonstrated by Fang *et al.* [30], to reduce the ancilla qubit requirements exponentially. Achieving an $O(1)$ success probability then requires $O(Q)$ applications of this block encoding [26], quadratically improving the average gate requirements over postselection. The overall CNOT gate complexity including amplitude amplification is $O(2^{p/2}t^{1+1/p}\epsilon^{-1/p}Q[G_U + G_D])$.

For the damped wave equation in d dimensions, $G_U = O(\log N)$, and $G_D = O(1)$, so the CNOT gate complexity is $O(2^{p/2}t^{1+1/p}\epsilon^{-1/p}Q\log N)$. Here, N is the total number of grid points across all spatial dimensions. Using the example of scalar transport in a laminar shear flow presented by Pfeffer *et al.* [12], the unitary advection substage requires $O(h \log^{h+1} N)$ CNOT gates for the prescribed polynomial velocity profile order h , and the diffusion substage requires $O(\log^2 N)$ gates, so the CNOT gate complexity in this setting is $O(2^{p/2}t^{1+1/p}\epsilon^{-1/p}Qh \log^{h+1} N)$ for $h \geq 1$. If QFT operations are required to input or post-process the data, then the required number of CNOT gates has an additive $O(n \log[n/\epsilon]) = O(\log N[\log \log N + \log\{1/\epsilon\}])$ term, using the most efficient approximate QFT circuits [31].

Figure 1 uses the controlled $R_Y(\theta)$ gate, which can be factored into

$$(I \otimes R_Y[\frac{\theta}{2}]) \text{CNOT} (I \otimes R_Y[-\frac{\theta}{2}]) \text{CNOT},$$

requiring two CNOT gates [32]. We now derive the exact CNOT gate counts for a single step in d dimensions, where n is the number of qubits in the data register per spatial dimension. The wave evolution unitary $U_w(\zeta t)$ in Fig. 1a requires $2n+4$ CNOT gates, and the damping evolution requires just 2 CNOT gates. The high-order splitting steps require $(q-1)d$ wave evolutions and q damping evolutions, where q is the number of stages in the product formula. Therefore, high-order splitting for the damped wave equation requires $d(2n+4)(q-1) + 2q$ CNOT gates. Using $q = 5$ for order 4, this is $8nd + 16d + 10$ CNOT gates. Using $q = 16$ for order 6, this is $30nd + 60d + 32$ CNOT gates. This is also the expression for the circuit depth, as all CNOT gates act on, or are controlled by, the selector qubit $|sel\rangle_S$.

V. CONCLUSIONS

We have developed a stable, high-order operator splitting approach for simulating dissipative dynamics on quantum computers using product formulas with complex coefficients. The evolution generator is decomposed into Hermitian and anti-Hermitian components, which are typically much simpler to implement than the exact dynamics. When required, each component can be further split into sums of simpler terms and simulated using an appropriate product formula with the same order. The resulting algorithm realises the dissipative dynamics as a sequence of simple Hamiltonian evolutions in real and imaginary time, with a composition that achieves high-order accuracy. This extends the flexibility and accuracy of high-order splitting methods for simulating unitary dynamics on quantum computers to dissipative dynamics, which are ubiquitous across computational science.

We have demonstrated the method by introducing pseudo-spectral quantum circuits for the damped wave equation, and by executing them on the IonQ Forte 1 trapped-ion quantum processor using product formulas up to order 6. The order-4 integrator produced more accurate dynamics than the corresponding integrators of orders 1 and 2, while also yielding success probabilities that were closer to the ideal contractive evolution. This indicates that, despite the increased circuit depth, higher-order splitting can deliver a practical accuracy advantage on near-term devices for dissipative dynamics.

Noise-free statevector simulations confirmed the convergence behaviour for all qualifying product formulas up to order 6. High-order product formulas significantly

reduced the number of CNOT gates required to achieve high precision, while maintaining gate counts comparable to low-order formulas in the low-precision regime. This suggests that high-order splitting can be chosen robustly across error tolerances, rather than being restricted to only high-precision regimes.

The overall CNOT gate count for p -order splitting scales as $O(2^{p/2}t^{1+1/p}\epsilon^{-1/p}Q[G_U + G_D])$, where Q quantifies the extent of the non-unitary dynamics, and G_U and G_D are the costs of implementing the individual unitary and dissipative substages, respectively. For order 6, this results in a near-linear $O(t^{7/6})$ dependence on the simulation time, and a rapidly diminishing dependence on the error $O(\epsilon^{-1/6})$. This is a substantial improvement over the existing order-2 approach with $O(t^{3/2})$ and $O(\epsilon^{-1/2})$ dependences.

Identifying qualifying operator splitting coefficients beyond order 6, and proving their existence in general, is a valuable area of future work. Relaxing the requirement for $b_j > 0$ for evolving the unitary dynamics may ease the discovery of higher-order product formulas. It remains to be determined whether qualifying product formulas beyond order 6 exhibit the same reliable convergence and low CNOT gate counts in practical implementations. While the presented method applies to general dissipative linear dynamics, its efficiency relies on either directly simulating the substages $e^{H_1 a_j \Delta t}$ and $e^{i H_2 b_j \Delta t}$ efficiently, or on being able to further decompose them efficiently. Therefore, developing techniques to perform the evolutions, either directly or by further decomposition, will enable the benefits to be realised across a wider range of applications and industries.

[1] S. Lloyd, Universal quantum simulators, *Science* **273**, 1073 (1996).

[2] M. Kliesch, T. Barthel, C. Gogolin, M. Kastoryano, and J. Eisert, Dissipative quantum church-turing theorem, *Physical Review Letters* **107**, 120501 (2011).

[3] G. Lindblad, On the generators of quantum dynamical semigroups, *Communications in mathematical physics* **48**, 119 (1976).

[4] Y. Ma and M. Kim, Limitations of probabilistic error cancellation for open dynamics beyond sampling overhead, *Physical Review A* **109**, 012431 (2024).

[5] A. M. Childs and Y. Su, Nearly optimal lattice simulation by product formulas, *Physical Review Letters* **123**, 050503 (2019).

[6] M. E. Morales, P. Costa, G. Pantaleoni, D. K. Burgarth, Y. R. Sanders, and D. W. Berry, Selection and improvement of product formulae for best performance of quantum simulation, *Quantum Information & Computation* **25**, 1 (2025).

[7] M. Suzuki, General decomposition theory of ordered exponentials, *Proceedings of the Japan Academy, Series B* **69**, 161 (1993).

[8] S. Blanes and F. Casas, On the necessity of negative co-efficients for operator splitting schemes of order higher than two, *Applied Numerical Mathematics* **54**, 23 (2005).

[9] D. Camps, L. Lin, R. Van Beeumen, and C. Yang, Explicit quantum circuits for block encodings of certain sparse matrices, *SIAM Journal on Matrix Analysis and Applications* **45**, 801 (2024).

[10] A. M. Childs and T. Li, Efficient simulation of sparse markovian quantum dynamics, *Quantum Information & Computation* **17**, 901 (2017).

[11] J. Ostmeyer, Optimised trotter decompositions for classical and quantum computing, *Journal of Physics A: Mathematical and Theoretical* **56**, 285303 (2023).

[12] P. Pfeffer, P. Brearley, S. Laizet, and J. Schumacher, Spectral quantum algorithm for passive scalar transport in shear flows, *Scientific Reports* **15**, 41172 (2025).

[13] D. An, J.-P. Liu, and L. Lin, Linear combination of Hamiltonian simulation for nonunitary dynamics with optimal state preparation cost, *Physical Review Letters* **131**, 150603 (2023).

[14] S. Jin, N. Liu, and Y. Yu, Quantum simulation of partial differential equations: Applications and detailed analysis, *Physical Review A* **108**, 032603 (2023).

[15] J. Hu, S. Jin, N. Liu, and L. Zhang, Quantum circuits

for partial differential equations via Schrödingerisation, *Quantum* **8**, 1563 (2024).

[16] G. H. Low and I. L. Chuang, Optimal Hamiltonian simulation by quantum signal processing, *Physical Review Letters* **118**, 010501 (2017).

[17] M. Motta, C. Sun, A. T. Tan, M. J. O'Rourke, E. Ye, A. J. Minnich, F. G. Brandao, and G. K.-L. Chan, Determining eigenstates and thermal states on a quantum computer using quantum imaginary time evolution, *Nature Physics* **16**, 205 (2020).

[18] A. Gilyén, Y. Su, G. H. Low, and N. Wiebe, Quantum singular value transformation and beyond: exponential improvements for quantum matrix arithmetics, in *Proceedings of the 51st Annual ACM SIGACT Symposium on Theory of Computing* (2019) pp. 193–204.

[19] J. Bernier, S. Blanes, F. Casas, and A. Escorihuela-Tomàs, Symmetric-conjugate splitting methods for linear unitary problems, *BIT Numerical Mathematics* **63**, 58 (2023).

[20] J.-S. Chen, E. Nielsen, M. Ebert, V. Inlek, K. Wright, V. Chaplin, A. Maksymov, E. Páez, A. Poudel, P. Maunz, *et al.*, Benchmarking a trapped-ion quantum computer with 30 qubits, *Quantum* **8**, 1516 (2024).

[21] G. Strang, On the construction and comparison of difference schemes, *SIAM Journal on Numerical Analysis* **5**, 506 (1968).

[22] F. Castella, P. Chartier, S. Descombes, and G. Vilmart, Splitting methods with complex times for parabolic equations, *BIT Numerical Mathematics* **49**, 487 (2009).

[23] H. Yoshida, Construction of higher order symplectic integrators, *Physics Letters A* **150**, 262 (1990).

[24] S. Blanes, F. Casas, and A. Murua, Splitting methods with complex coefficients, *SeMA Journal* **50**, 47 (2010).

[25] R. I. McLachlan, On the numerical integration of ordinary differential equations by symmetric composition methods, *SIAM Journal on Scientific Computing* **16**, 151 (1995).

[26] G. Brassard, P. Høyer, M. Mosca, and A. Tapp, Quantum amplitude amplification and estimation, *Contemporary Mathematics* **305**, 53 (2002).

[27] G. Strang, The discrete cosine transform, *SIAM Review* **41**, 135 (1999).

[28] A. Klappenecker and M. Rötteler, Discrete cosine transforms on quantum computers, in *ISPA 2001 – Proceedings of the 2nd International Symposium on Image and Signal Processing and Analysis, in conjunction with the 23rd International Conference on Information Technology Interfaces (ITI 2001)* (2001) pp. 464–468.

[29] J. P. Gaebler, C. H. Baldwin, S. A. Moses, J. M. Dreiling, C. Figgatt, M. Foss-Feig, D. Hayes, and J. M. Pino, Suppression of midcircuit measurement crosstalk errors with micromotion, *Physical Review A* **104**, 062440 (2021).

[30] D. Fang, L. Lin, and Y. Tong, Time-marching based quantum solvers for time-dependent linear differential equations, *Quantum* **7**, 955 (2023).

[31] R. Cleve and J. Watrous, Fast parallel circuits for the quantum Fourier transform, in *Proceedings 41st Annual Symposium on Foundations of Computer Science* (IEEE, 2000) pp. 526–536.

[32] A. Barenco, C. H. Bennett, R. Cleve, D. P. DiVincenzo, N. Margolus, P. Shor, T. Sleator, J. A. Smolin, and H. Weinfurter, Elementary gates for quantum computation, *Phys. Rev. A* **52**, 3457 (1995).

ACKNOWLEDGMENTS

Peter Brearley is supported by The University of Manchester via the Dame Kathleen Ollerenshaw Fellowship and the National Quantum Computing Centre [NQCC200921], which is a UKRI Centre and part of the UK National Quantum Technologies Programme (NQTP). Philipp Pfeffer is supported by the European Union (ERC, MesoComp, 101052786). Views and opinions expressed are however those of the author(s) only and do not necessarily reflect those of the European Union or the European Research Council. Neither the European Union nor the granting authority can be held responsible for them.